

Quasi-two-dimensional relativistic fermions probed by de Haas–van Alphen quantum oscillations in LuSn₂

Yanglin Zhu¹, Jin Hu^{2,3}, David Graf⁴, Xin Gui⁵, Weiwei Xie⁶, and Zhiqiang Mao^{1,*}

¹*Department of Physics, Pennsylvania State University, University Park, Pennsylvania 16802, USA*

²*Department of Physics, University of Arkansas, Fayetteville, Arkansas 72701, USA*

³*Institute for Nanoscience and Engineering, University of Arkansas, Fayetteville, Arkansas 72701, USA*

⁴*National High Magnetic Field Laboratory, Tallahassee, Florida 32310, USA*

⁵*Department of Chemistry, Louisiana State University, Baton Rouge, Louisiana 70803, USA*

⁶*Department of Chemistry and Chemical Biology, Rutgers University, Piscataway, New Jersey 08854, USA*



(Received 6 October 2020; accepted 16 February 2021; published 4 March 2021)

We report de Haas–van Alphen (dHvA) quantum oscillation studies on a layered compound LuSn₂. Through the analyses of the dHvA oscillation data, we find this material has several 3D bands and one quasi-2D band hosting relativistic fermions. Compared to previously reported dHvA oscillations in YSn₂, the oscillation component arising from the quasi-2D band is significantly enhanced. From structural analyses using single-crystal x-ray diffraction, we find the distorted Sn-square net layer is less corrugated than YSn₂, which accounts for the enhancement of two dimensionality of the relativistic fermions created in this layer. This result suggests that the dimensionality of relativistic band in RESn₂ (RE = rare earth) can be tuned by electronegativity of RE. Moreover, we also find the 3D relativistic bands are pushed closer to the Fermi level with respect to YSn₂, due to enhanced spin-orbital coupling. These findings imply RESn₂ can be an interesting platform for seeking new topological states via the tuning of electronegativity, spin-orbital coupling, and magnetism.

DOI: [10.1103/PhysRevB.103.125109](https://doi.org/10.1103/PhysRevB.103.125109)

I. INTRODUCTION

Three-dimensional topological materials, including Dirac [1–6], Weyl [7–14], and nodal-line semimetals [15–17], possess linear band-crossing points, i.e., Dirac/Weyl points, in their bulk electronic band structure. The quasiparticles excited near the Dirac or Weyl points can be described as relativistic fermions, which can give rise to striking exotic properties, such as large magnetoresistance [18–24], high transport mobility [18,25], and chiral anomaly [24,26,27]. Among current 3D topological materials, one class of materials features layered structures and their topological states are created by 2D square lattices or distorted square lattices formed by group IV or V elements. The examples include ATX_2 ($A = \text{Ca, Sr, Ba, or rare earth, } T = \text{Mn, Zn, or Ag; } X = \text{Bi or Sb}$) [28–38], and WHM ($W = \text{Zr, Hf, or rare-earth elements; } H = \text{Si, Ge, Sn, Sb; and } M = \text{S, Se, Te}$) [39–48]. A variety of unique topological semimetal states has been observed in these materials, such as the anisotropic Dirac cone state in SrMnBi₂ [28], the nodal line, and 2D nonsymmorphic Dirac states in ZrSi(S/Se/Te) [39,40,42,49–53], the Dirac state with spin-valley locking in BaMnSb₂ [54]. Moreover, magnetism can also be present in some members of the ATX_2 and WHM families, in which the interplay between magnetism and nontrivial bands may generate even more exotic states, e.g., the time-reversal symmetry-breaking Weyl state in YbMnBi₂ [38], the bulk quantum Hall effect in EuMnBi₂ [55], magnetically

tuned Dirac state in SrMnSb₂ [33], and tunable Weyl and Dirac states in CeSbTe [44].

In addition to Si, Sb, and Bi square lattices, square or distorted square lattice of Sn has also been demonstrated to generate topological states. Examples include ZrSnTe [46,48] and YSn₂ [56]. ZrSnTe belongs to the WHM family with Sn square net that creates topological surface states [46], whereas the Sn square lattice in YSn₂ is distorted and forms non-centrosymmetric orthorhombic structure. Earlier de Haas–van Alphen (dHvA) quantum oscillation studies on YSn₂ [56] revealed multiple topological nontrivial bands, including a 3D band hosting a possible tunable Weyl state and a quasi-2D band. While the 3D Weyl band is predicted theoretically, the origin of the quasi-2D band remains elusive [56].

In this work, we have performed dHvA quantum oscillation studies on LuSn₂. Although it shares a similar structure with YSn₂, the relatively larger electronegativity and stronger SOC of Lu would possibly affect its electronic states. In our experiments, we observed very strong dHvA oscillations in LuSn₂ single crystals. Interestingly, the oscillation component arising from the quasi-2D band is much stronger than that due to the 3D bands, in stark contrast with the scenario seen in YSn₂, where the oscillation component from the quasi-2D band is much weaker than that of the 3D band [56]. Additionally, compared to YSn₂, the 3D non-trivial bands in LuSn₂ are pushed closer to the Fermi level. From single crystal structural analyses, we find the Sn square lattice is much less distorted than that of YSn₂, thus enhancing the two-dimensionality of the bands arising from the Sn 2D layer. This explains the significant enhancement of the dHvA oscillations originating

*zim1@psu.edu

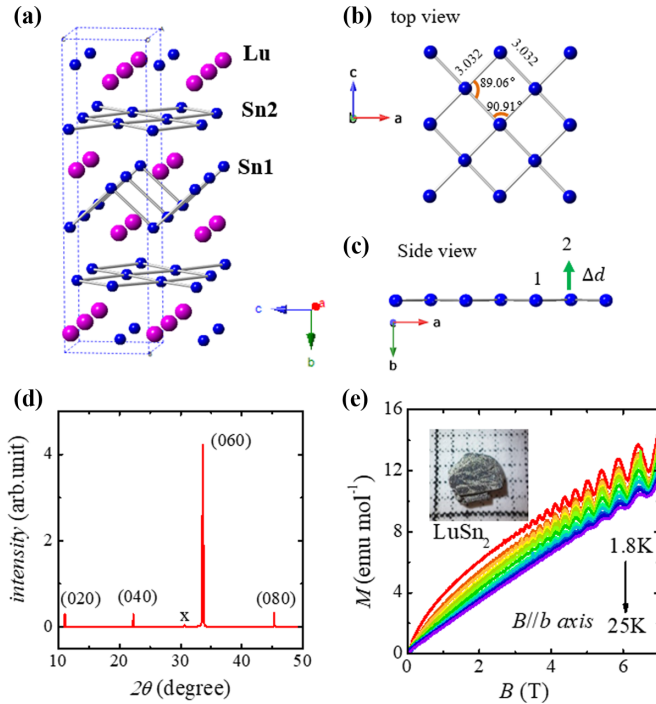


FIG. 1. (a) Crystal structure of LuSn_2 ; top (b) and side (c) view of the distorted Sn square net layer. Δd in (c) represents the relative displacement of Sn2 atoms along the b axis. (d) Single-crystal x-ray-diffraction spectra of LuSn_2 . A small peak marked as “x” is due to the residual Sn flux on the surface. (e) Isothermal out of plane ($B||b$ axis) magnetization M for LuSn_2 at various temperatures (from 1.8 to 25 K). Inset: an optical image of a LuSn_2 single crystal.

from the quasi-2D band. These results not only demonstrate an effective pathway of non-trivial band tuning through controlling electronegativity and spin-orbital coupling (SOC), but also suggest RESn_2 ($\text{RE} = \text{rare earth}$) could be an interesting platform for seeking novel topological states through tuning of electronegativity, SOC, and magnetism.

II. METHODS

The LuSn_2 single crystals were synthesized using a metal flux method. The Lu pieces and Sn lumps with the molar ratio of 1:10 were loaded in an Al_2O_3 crucible and sealed in a quartz tube under high vacuum. The mixture was heated to 1050 °C, held at this temperature for 48 h for homogeneous melting, and slowly cooled down to 750 °C at a rate of 2 °C per hour. The platelike single crystals with silver luster [see inset of Fig. 1(e)] can be obtained after removing the excess Sn flux by centrifugation. The composition of the grown crystals was confirmed to be approximately stoichiometric using an energy-dispersive x-ray spectrometer. The excellent crystallization of the single crystals was verified by the sharp (0K0) x-ray-diffraction peaks [Fig. 1(d)]. The crystal structure of the grown crystals was characterized using single-crystal x-ray diffraction, as presented below. The magnetization was measured using a superconducting quantum interference device (SQUID) magnetometer (Quantum Design), and the magnetic torque measurements were carried out at the National High

TABLE I. lattice parameters derived from single-crystal XRD measurements at 200(2) K. Space group: $Cmcm$ (No. 63). Lattice parameters: $a = 4.3326(8)$ Å, $b = 15.9730(3)$ Å, $c = 4.2525(7)$ Å, $\alpha = \beta = \gamma = 90^\circ$. ($R_1 = 3.89\%$, $wR_2 = 6.64\%$, goodness of fit = 1.043 with 2357 total reflections).

Atom	Wyckoff	Occupancy	x	y	z	U_{eq}
Lu	4a	1	0	0.4017(1)	¼	0.0070(3)
Sn1	4a	1	0	0.0643(1)	¼	0.0080(4)
Sn2	4a	1	0	0.7514(1)	¼	0.0069(5)

Magnetic Field Lab (NHMFL) in Tallahassee using a cantilever torque magnetometer.

III. RESULTS AND DISCUSSION

A. Structure determination of LuSn_2

Single-crystal x-ray-diffraction data were collected at 200, 150, and 115 K on a Bruker Apex II diffractometer with Mo radiation $K\alpha_1$ ($\lambda = 0.71073$ Å) and refined with the SHELXTL package. The best refinement of the single-crystal x-ray spectra on LuSn_2 indicates the structure with a space group $Cmcm$ which is consistent with the previous report [57]. The details of structural parameters are summarized in Table I. Similar to YSn_2 , the structure of LuSn_2 can be viewed as stacking of $[\text{Lu}_2^{3+}\text{Sn}_2^{2-}]$ blocks and Sn planes. The Sn square net in YSn_2 is distorted with the bonding angles slightly deviating from 90° (88.68° and 91.27°). In contrast, in LuSn_2 , the bonding angle between the Sn-Sn bonds of the Sn square net is closer to 90° , i.e., 89.06° and 90.91° , as shown in the top view of the distorted Sn square net [Fig. 1(b)]. From the side view of the square plane [Fig. 1(c)], we find that the Sn atoms form 2D planes with very small corrugation. The relative displacement Δd of Sn atoms of the 2D Sn layer along the b axis is 0.048 Å in LuSn_2 [Fig. 1(c)], smaller than that in YSn_2 (0.061 Å). This suggests that the Sn square net in LuSn_2 is less corrugated than that in YSn_2 . This is consistent with our dHvA oscillation observations (see below), which suggests that Sn square lattice hosting the topological state becomes more 2D-like in LuSn_2 .

B. Relativistic fermions in LuSn_2 probed by dHvA oscillations

Signatures of topological relativistic fermions in LuSn_2 , including light effective mass, high mobility, and nontrivial Berry phase, have been extracted from our dHvA quantum oscillation studies on single crystals. We have observed clear dHvA oscillations in the isothermal magnetization measurements using a SQUID magnetometer. As shown in Fig. 1(e), when the magnetic field was applied along the out of plane direction (i.e., $B||b$ axis), the magnetization at 1.8 K starts to show oscillations above 3 T, and the oscillations remain discernible up to 25 K. Such oscillations become more conspicuous after removing the nonoscillation background, as shown in Fig. 2(a). A single oscillation frequency of 70 T (denoted by F_β^{Lu} below) can be extracted from the fast Fourier transform (FFT) analyses, as shown in the inset of Fig. 2(b). For in-plane magnetic field, however, no oscillation can be probed up to 7 T (the highest field which can be achieved in

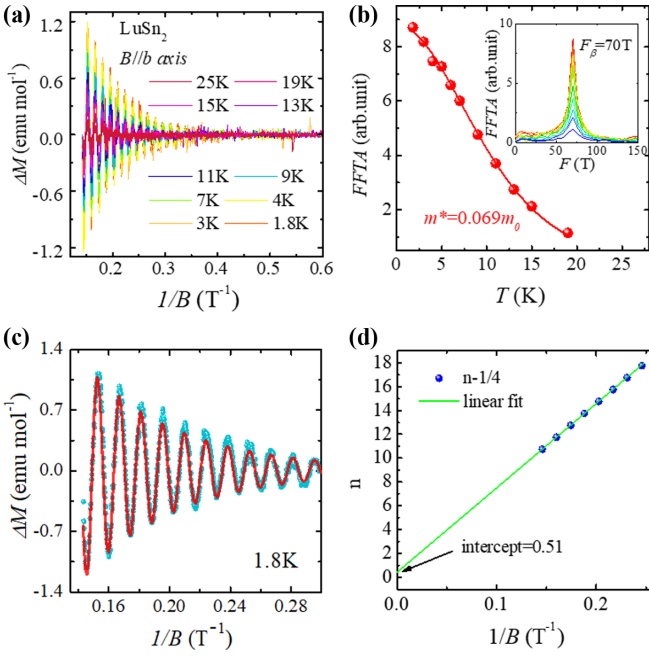


FIG. 2. (a) Oscillatory magnetization ΔM obtained by subtracting the nonoscillating background for $B||b$ in the 1.8–25 K temperature range. (b) The fit of the FFT amplitudes of the dHvA oscillations to the temperature damping factor R_T in the LK formula. Inset shows the FFT spectra of the oscillatory magnetization for $B||b$. (c) The fit (red line) of the dHvA oscillation pattern (blue dots) at 1.8 K to the LK formula. (d) Landau index fan diagram and the linear fit. The blue solid circle represents the minima of ΔM .

our SQUID), consistent with the 2D-like electronic structure expected for layered materials. This is also confirmed by Fermi surface morphology revealed by the angular dependence of dHvA oscillation measurements, as will be discussed below.

We can extract further information about the relativistic fermions from analyses of dHvA oscillations. The dHvA oscillations can be described by the Lifshitz-Kosevich (LK) formula [58,59], with a Berry phase being taken into account:

$$\Delta M \propto -B^{1/2} R_T R_D R_S \sin \left[2\pi \left(\frac{F}{B} + \gamma - \delta \right) \right], \quad (1)$$

where $R_T = \alpha T m^* / [B m_0 \sinh(\alpha T m^* / B m_0)]$, $R_D = \exp(-\alpha T_D m^* / B m_0)$ and $R_S = \cos(\pi g m^* / 2 m_0)$. The α is a constant which equals $(2\pi^2 k_B m_0) / (\hbar e)$ and T_D is the Dingle temperature. The $\gamma - \delta$ is the phase factor, in which $\gamma = \frac{1}{2} - \frac{\phi_B}{2\pi}$ and ϕ_B is Berry phase. The phase shift δ is determined by the dimensionality of the Fermi surface (FS); δ equals 0 and $\pm 1/8$ for 2D and 3D cases, respectively, with the sign depending on whether the probed extreme cross-section area of the FS is maximal (–) or minimal (+).

From the LK formula, the effective mass m^* of quasiparticles can be estimated from the fit of the temperature dependence of the oscillation amplitude by the thermal damping factor R_T . As shown in Fig. 2(b), which plots the temperature dependence of the FFT oscillation amplitude, the fit yields a small effective mass, $\sim 0.069 m_0$ (m_0 , free-electron mass). With the known parameters of effective masses and os-

cillation frequency, we have further fitted the dHvA oscillation patterns at 1.8 K to the LK-formula, as shown in Fig. 2(c). From the fit, we have extracted the Dingle temperature of 10 K, from which the quantum mobility $\mu_q [= e\hbar / (m^* 2\pi k_B T_D)]$ is estimated to be $3102 \text{ cm}^2 \text{ V}^{-1} \text{ s}^{-1}$.

Besides the light effective mass and high quantum mobility, the nontrivial Berry phase Φ_B is also extracted by LK formula fitting and Landau level (LL) index fan diagram, as shown in Figs. 2(c) and 2(d). Through the above LK-formula fitting [Fig. 2(c)], the extracted phase factor is $\gamma - \delta = 0.048$, from which the Berry phase of $(0.452 - \delta) \times 2\pi$ can be derived. The measurements of angular dependence of dHvA oscillations presented later indicate that the band with the oscillation frequency of F_β^{Lu} exhibits 2D characteristics, implying that δ should be taken as 0 and thus the Berry phase is 0.904π , close to the ideal value of π for nontrivial topological bands. To further verify the Berry phase, we also performed the LL index fan diagram fitting, as shown in Fig. 2(d). In general, for a system exhibiting quantum oscillations with a single frequency, the Berry phase can be determined from the LL index fan diagram, i.e., the plot of the Landau indices n versus the inverse magnetic field $1/B$, and the linear extrapolation should intercept the n axis at $\frac{\phi_B}{2\pi} - \delta$. According to customary practice, integer LL indices should be assigned when the density of state at the Fermi level DOS (E_F) reaches a minimum. For dHvA oscillations, the oscillatory susceptibility χ is proportional to the oscillatory DOS (E_F). Given that χ is the derivative of magnetization M , the minima of the magnetization and susceptibility are shifted by $\pi/2$. Therefore, when the oscillations of magnetization are used for determining the LL fan diagram, the minima of M should be assigned with $n - 1/4$ (where n is an integer number) [42,59,60]. Through this approach, the intercept to the n axis is determined to be 0.51; thus the Berry phase is 1.02π , which is in good agreement with the value determined from the LK fitting.

Although the dHvA oscillations measured in low magnetic field range only revealed a single frequency, it may not indicate that the LuSn₂ is single-band system. To obtain more comprehensive information on electronic band structure, we have further performed magnetic torque measurements up to 31 T on LuSn₂ at the NHMFL. It is worth pointing out that the torque signal is expected to vanish when the magnetic field is exactly aligned along the out of plane ($B||b$ axis) and in plane ($B||ac$ plane) direction. To obtain finite torque signal, we performed the magnetic torque measurements with field nearly along the b axis and ac plane, which are denoted by $B||b'$ and $B||ac'$, respectively. We indeed observed multiple oscillation frequencies in high-field torque measurements. As shown in Fig. 3(a), for $B||b'$, at $T = 1.8$ K, the oscillations exhibit single frequency at low field, and two additional high frequencies components start to appear for $B > 12$ T. The FFT analyses [inset of Fig. 3(b)] reveal three frequencies: $F_\beta^{\text{Lu}} = 70$ T (i.e., the one probed by the SQUID magnetometer), and two additional higher frequencies $F_\gamma^{\text{Lu}} = 422$ T and $F_\theta^{\text{Lu}} = 511$ T. The fit of the temperature dependence of FFT amplitudes to the R_T yields an effective electron mass of $0.053 m_0$ for the β band, as shown in Fig. 3(b). This value is smaller than that obtained from the SQUID magnetometer measurements noted above ($0.069 m_0$). Such a discrepancy is likely caused by the fewer data points for torque measurements. For the bands with

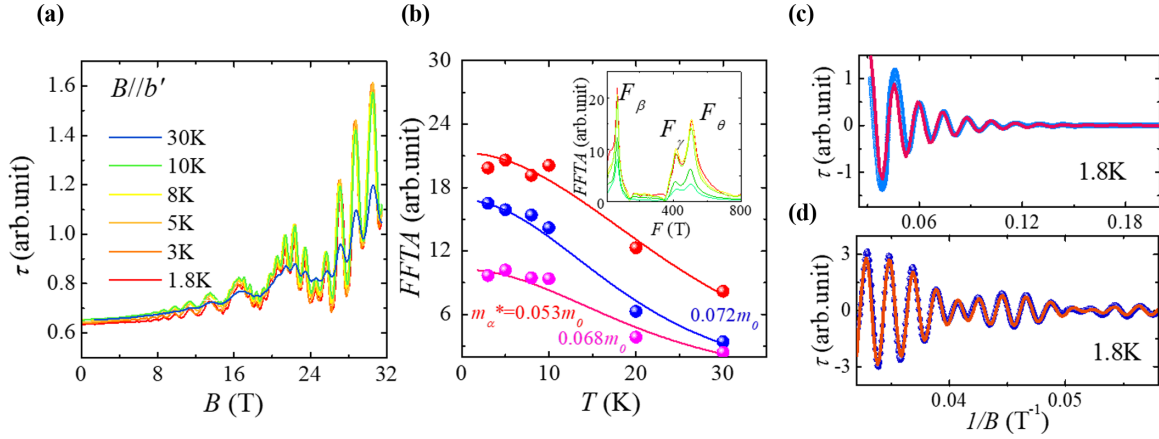


FIG. 3. (a) The field dependence of magnetic torque τ for LuSn_2 at different temperatures from 1.8 to 30 K, which show strong dHvA oscillations. The magnetic field is applied nearly along the b axis ($B||b'$). (b) The fits of the FFT amplitudes to the temperature-damping term R_T of the LK formula. Inset shows the FFT spectra of the oscillatory magnetization $\Delta\tau$ for $B||b'$ axis. (c) The low-frequency (F_β) dHvA oscillations probed in magnetic torque for $B||b'$ axis obtained after filtering the high-frequency components. (d) The high-frequency (F_γ and F_θ) oscillatory components of magnetic torque obtained after filtering the low-frequency component. The solid curves in (c) and (d) represent the fits of the $T = 1.8$ K oscillation patterns by the LK formula.

high frequency F_γ^{Lu} and F_θ^{Lu} , we obtained comparable light effective masses, i.e., $m_\gamma^* = 0.068m_0$ and $m_\theta^* = 0.072m_0$.

To further evaluate the properties of quasiparticles hosted by the β -, γ -, and θ bands, we have performed the LK fit for the $T = 1.8$ K oscillatory torque components obtained by subtracting the nonoscillating background. To minimize fitting parameters, we have separated the F_β^{Lu} component from the F_γ^{Lu} and F_θ^{Lu} components. The fit shown in Fig. 3(c) is made for the single F_β^{Lu} component. The LK fit yields Berry phase to be 0.996π , which is consistent with the value extracted from the dHvA oscillation pattern measured by the SQUID magnetometer. This result further supports the nontrivial topological nature of the β band in LuSn_2 . For the high-frequency components (F_γ^{Lu} and F_θ^{Lu}) shown in Fig. 3(d), the oscillation pattern at $T = 1.8$ K can be fitted well by the two-band LK model. From this fit, we obtained nontrivial Berry phases, $(0.598 \pm 0.25)\pi$ and $(1.038 \pm 0.25)\pi$ for the γ - and θ bands, as listed in Table II. As shown below, the γ - and θ bands display the 3D nature so that δ is taken as $\pm 1/8$ in their Berry phase's estimate. This result suggests that all three bands probed by the dHvA oscillations host relativistic fermions. Other signatures of relativistic fermions, such as high quantum mobility, are also revealed by LK fits, as summarized in Table II.

In addition to elucidating the nontrivial nature of multiple bands in LuSn_2 , we also investigated the Fermi-surface morphology by measuring the angular dependences of the quantum oscillations. In Fig. 4, we present two sets of angular dependences of quantum oscillation, which are measured by the SQUID magnetometer [Fig. 4(a)] and magnetic torque [Fig. 4(c)], respectively. The F_β^{Lu} oscillation component is probed in both magnetization and torque measurements. The backgrounds have been subtracted for the data presented in Figs. 4(a) and 4(c). As shown in Fig. 4(a), for $B||b'$, the low-field oscillation pattern obtained by the SQUID magnetometer only contains the single-frequency F_β^{Lu} . When the field starts to rotate away from the b axis (i.e., toward in-plane direction), the oscillation is gradually suppressed and finally disappears at the rotation angle of $\vartheta > 44^\circ$. Such an evolution of F_β^{Lu} is also reproduced by the magnetic torque measurements [Fig. 4(c)]. We summarized the angular-dependent F_β^{Lu} in Fig. 4(b), where the black hollow and solid circles represent the data measured by SQUID magnetometer and torque, respectively. The data can be well fitted to a $1/\cos\theta$ dependence, suggesting the quasi-2D nature of the F_β^{Lu} band. In Fig. 4(b) we also include the angular dependences of the other two higher-frequency branches F_γ^{Lu} and F_θ^{Lu} . Both of them are present in the full angular range up to 90° , indicating the 3D nature of these two bands.

TABLE II. Parameters derived from the analyses of dHvA oscillations for LuSn_2 . F , oscillation frequency; T_D , Dingle temperature; m^* , effective mass; μ_q , quantum mobility; Φ_B , Berry phase; δ , the phase-shift factor in quantum oscillations; $\delta = 0$ for a 2D FS, but $\pm 1/8$ for a 3D FS (see text).

	$F(\text{T})$	Notation	$T_D(\text{K})$	m^*/m_0	$\mu_q(\text{cm}^2/\text{Vs})$	Φ_B		
						$\delta = 1/8$	$\delta = 0$	$\delta = -1/8$
$B b$ (M)	70	F_β^{Lu}	10	0.069	3102	0.654π	0.904π	1.154π
$B b'$ (torque)	70	F_β^{Lu}	49	0.053	824	0.764π	0.996π	1.246π
	422	F_γ^{Lu}	78	0.068	401	0.348π	0.598π	0.848π
	511	F_θ^{Lu}	123	0.072	240	0.788π	1.038π	1.288π

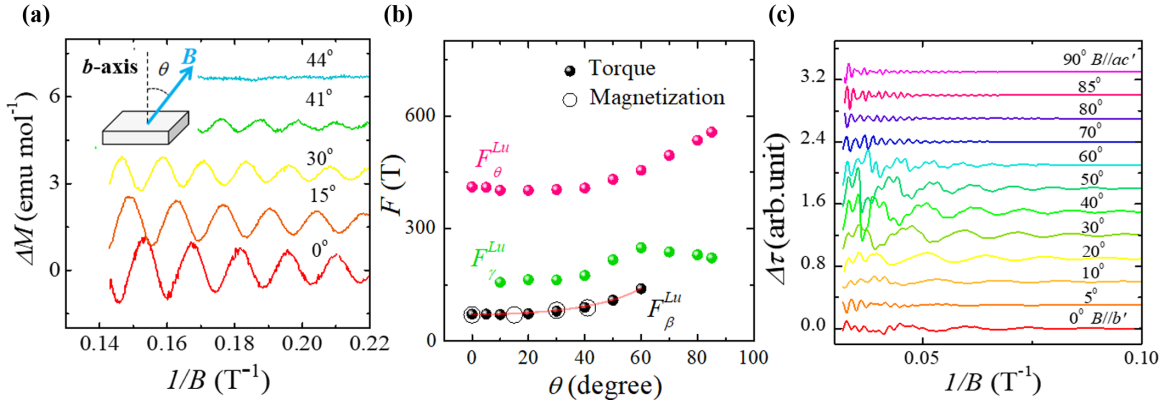


FIG. 4. (a) dHvA oscillations of isothermal magnetization (M) for LuSn_2 at $T = 1.8$ K under different magnetic field orientations. Inset: the experimental setup. (b) The angular dependences of oscillation frequencies for LuSn_2 . (c) dHvA oscillations of magnetic torque at $T = 1.8$ K under different magnetic field orientations for LuSn_2 . The data of different θ have been shifted for clarity and the nonoscillating background has been subtracted.

C. Discussion

From the above dHvA oscillation analysis, we conclude that LuSn_2 hosts three topological-nontrivial bands, i.e., the quasi-2D β_{Lu} band and 3D γ_{Lu} and θ_{Lu} bands. The properties of relativistic fermions hosted by these bands are manifested by light effective mass ($0.069\text{--}0.072 m_0$), high quantum mobility, and nontrivial Berry phase. Although these relativistic fermions' properties are similar to those of YSn_2 , [56], the electronic band structure of LuSn_2 shows distinct characteristic, as discussed below. YSn_2 involves five nontrivial topological bands, i.e., one quasi-2D band (β_Y) and four 3D anisotropic bands (α_Y , γ_Y , θ_Y , and ϕ_Y) [56]. Theory predicts that the α_Y band hosts a new type of Weyl state caused by Rashba spin-orbital coupling. The 3D γ_Y , θ_Y , and ϕ_Y bands probed in the dHvA oscillations are also verified in the band-structure calculations. However, the quasi-2D β_Y band was not identified in the band-structure calculations, the reason of which is that the calculated band with quasi-2D character forms a Fermi-surface sheet with an extremely complicated geometric shape and has strong anisotropy (Fig. 7(b) in Ref. [56]). Although the large portion of this pocket is open, it can possibly form a small closed cyclotron orbit corresponding to the probed frequency F_β^Y at a certain k_y when the magnetic field is applied along the b axis. But, quantitative determination of the extremal cyclotron orbit for this quasi-2D, complicated Fermi-surface sheet is difficult, since it is not on a high symmetric plane. Given the structural similarity between LuSn_2 and YSn_2 , it is reasonable to assume LuSn_2 shares some similarity in band structure with YSn_2 . This is indeed verified by the fact that both the γ - and θ pockets are probed in both LuSn_2 and YSn_2 , though the size of these pockets becomes larger in LuSn_2 . Therefore, the quasi-2D β band of LuSn_2 probed in our dHvA experiments likely has similar nature with that in YSn_2 , i.e., this band forms the extremely anisotropic Fermi surface.

In LuSn_2 , while the α band is not probed, the oscillation component due to the quasi-2D β band is significantly enhanced as compared to YSn_2 . We observed a remarkable increase in the amplitude of dHvA oscillation of the β band, which is almost two times larger than that of the γ band [see

the inset to Fig. 3(b)]. In contrast, the torque measurements on YSn_2 , barely probed the quasi-2D β band for $B||b'$, although it is observed in magnetization measurements (see Fig. 3(b) in Ref. [56]). Such a significant enhancement of the quantum oscillation amplitude suggests that the two dimensionality of the β band in LuSn_2 is greatly increased when compared with YSn_2 , since 2D bands are generally known to generate much stronger quantum oscillations than 3D bands [59,61].

The increase of the two dimensionality of the β band in LuSn_2 can be attributed to the fact that the electronegativity difference between Lu and Sn is larger than the one between Y and Sn. As noted above, YSn_2 , or LuSn_2 is characterized by the distorted Sn2 square lattice, which is sandwiched by two (Y/Lu)Sn1 blocks, as shown in Fig. 1(a). The Y atom is coordinated with six Sn1 (Sn atoms in YSn block) and four Sn2 atoms. Due to the relatively weak electronegativity of Y atom, it prefers to form the more covalent bonds with the Sn2 atoms of the square net. Such covalent bonds between Y and Sn2 atoms distort the square net of Sn2, which in turn weakens the two dimensionality of the nontrivial state created by the distorted Sn2 square net. In contrast, in LuSn_2 , since Lu is more electronegative than Y, Lu tends to form a more ionic bond with Sn2 than Y. The oxidation states of Lu and isolated Sn are +3 and -2 ; each Sn in the puckered 2D square network will be left with five valence electrons to form four equivalent Sn-Sn bonds. As such, each Sn will donate their unpaired electrons to the square network and be normal two-center two-electron (2c-2e) bonds. The observation of less-puckered Sn square planar with shorter Sn-Sn distance in LuSn_2 implies stronger 2c-2e bonds in LuSn_2 , thus more localized bonds in Sn square planar. In other words, the Sn square lattice becomes more isolated than that in YSn_2 . Therefore, the electronic bands hosted by such a square lattice naturally become more 2D-like.

Another noticeable difference between LuSn_2 and YSn_2 is their crystal symmetry: YSn_2 has a noncentrosymmetric orthorhombic structure with the space group of $Cmc2_1$, whereas LuSn_2 possesses a centrosymmetric orthorhombic structure ($Cmcm$). Such a crystal symmetry change leads to the absence of the 3D α band in LuSn_2 . However, other 3D bands, i.e., the γ - and θ bands, survive, but they are closer to the Fermi

level, as reflected in their higher dHvA frequencies. In LuSn₂, F_{γ}^{Lu} and F_{θ}^{Lu} are 422 and 511 T, respectively, much larger than those in YSn₂, ($F_{\gamma}^{\text{Y}} = 386$ T, $F_{\theta}^{\text{Y}} = 465$ T). The charge carriers hosted by the γ - and θ bands in LuSn₂, display heavier effective mass ($m_{\gamma}^* = 0.068 m_0$ and $m_{\theta}^* = 0.072 m_0$) and much lower quantum mobility ($\mu_{q,\gamma} = 401$ cm²/Vs, $\mu_{q,\theta} = 240$ cm²/Vs) as compared with YSn₂, ($m_{\gamma}^* = 0.023 m_0$ and $m_{\theta}^* = 0.038 m_0$; $\mu_{q,\gamma} = 767$ and $\mu_{q,\theta} = 891$ cm²/Vs) [56]. We believe the 3D γ - and θ bands should be generated by the p orbital of Sn1 atoms in Lu₂³⁺Sn₂²⁻ block, which are likely affected by the stronger SOC introduced by Lu.

IV. CONCLUSION

In summary, we have synthesized single crystals of LuSn₂, characterized its crystal structure using single-crystal XRD, and investigated its dHvA oscillations. We find that the Sn square net layer of LuSn₂ is less distorted than YSn₂. We observed strong dHvA oscillations in this material. From the analyses of the dHvA oscillation data, we have demonstrated that LuSn₂ has multiple bands hosting relativistic fermions, including two 3D bands and one quasi-2D band. Through comparison with YSn₂, we find the electronic band structure

of LuSn₂ exhibits distinct signatures due to the enhanced electronegativity and SOC of Lu. The two dimensionality of the β band is significantly enhanced in LuSn₂ than that in YSn₂, which can be attributed to the fact that large electronegativity of Lu causes less distortion of the Sn square net. These results indicate that, in the RESn₂ (RE = rare-earth) system, the variation of RE atom could affect the nature of 2D square net formed by Sn atoms, which could tune the topological properties of the bands generated by the Sn 2D square lattice.

ACKNOWLEDGMENTS

This work is supported by the US National Science Foundation under Grants No. DMR 1832031 and No. 1917579. A portion of this work was performed at the National High Magnetic Field Laboratory, which is supported by National Science Foundation Cooperative Agreement No. DMR-1644779 and the State of Florida. Y.Z. acknowledges partial financial support from the National Science Foundation (NSF) through the Penn State 2D Crystal Consortium-Materials Innovation Platform No. 2DCC-MIP under NSF Cooperative Agreement No. DMR-1539916. W.X. acknowledges the support from Grant No. NSF-DMR-1944965.

-
- [1] Z. Wang, Y. Sun, X.-Q. Chen, C. Franchini, G. Xu, H. Weng, X. Dai, and Z. Fang, *Phys. Rev. B* **85**, 195320 (2012).
- [2] Z. K. Liu, B. Zhou, Y. Zhang, Z. J. Wang, H. M. Weng, D. Prabhakaran, S.-K. Mo, Z. X. Shen, Z. Fang, X. Dai *et al.*, *Science* **343**, 864 (2014).
- [3] Z. Wang, H. Weng, Q. Wu, X. Dai, and Z. Fang, *Phys. Rev. B* **88**, 125427 (2013).
- [4] Z. K. Liu, J. Jiang, B. Zhou, Z. J. Wang, Y. Zhang, H. M. Weng, D. Prabhakaran, S. K. Mo, H. Peng, P. Dudin *et al.*, *Nat. Mater.* **13**, 677 (2014).
- [5] M. Neupane, S.-Y. Xu, R. Sankar, N. Alidoust, G. Bian, C. Liu, I. Belopolski, T.-R. Chang, H.-T. Jeng, H. Lin *et al.*, *Nat. Commun.* **5**, 3786 (2014).
- [6] S. Borisenko, Q. Gibson, D. Evtushinsky, V. Zabolotnyy, B. Büchner, and R. J. Cava, *Phys. Rev. Lett.* **113**, 027603 (2014).
- [7] S.-M. Huang, S.-Y. Xu, I. Belopolski, C.-C. Lee, G. Chang, B. Wang, N. Alidoust, G. Bian, M. Neupane, C. Zhang, S. Jia, A. Bansil, H. Lin, and M. Z. Hasan, *Nat. Commun.* **6**, 7373 (2015).
- [8] H. Weng, C. Fang, Z. Fang, B. A. Bernevig, and X. Dai, *Phys. Rev. X* **5**, 011029 (2015).
- [9] S.-Y. Xu, I. Belopolski, N. Alidoust, M. Neupane, G. Bian, C. Zhang, R. Sankar, G. Chang, Z. Yuan, C.-C. Lee *et al.*, *Science* **349**, 613 (2015).
- [10] B. Q. Lv, H. M. Weng, B. B. Fu, X. P. Wang, H. Miao, J. Ma, P. Richard, X. C. Huang, L. X. Zhao, G. F. Chen, Z. Fang, X. Dai, T. Qian, and H. Ding, *Phys. Rev. X* **5**, 031013 (2015).
- [11] B. Q. Lv, N. Xu, H. M. Weng, J. Z. Ma, P. Richard, X. C. Huang, L. X. Zhao, G. F. Chen, C. E. Matt, F. Bisti, V. N. Strocov, J. Mesot, Z. Fang, X. Dai, T. Qian, M. Shi, and H. Ding, *Nat. Phys.* **11**, 724 (2015).
- [12] L. X. Yang, Z. K. Liu, Y. Sun, H. Peng, H. F. Yang, T. Zhang, B. Zhou, Y. Zhang, Y. F. Guo, M. Rahn, D. Prabhakaran, Z. Hussain, S.-K. Mo, C. Felser, B. Yan, and Y. L. Chen, *Nat. Phys.* **11**, 728 (2015).
- [13] S.-Y. Xu, N. Alidoust, I. Belopolski, Z. Yuan, G. Bian, T.-R. Chang, H. Zheng, V. N. Strocov, D. S. Sanchez, G. Chang, C. Zhang, D. Mou, Y. Wu, L. Huang, C.-C. Lee, S.-M. Huang, B. Wang, A. Bansil, H.-T. Jeng, T. Neupert, A. Kaminski, H. Lin, S. Jia, and M. Z. Hasan, *Nat. Phys.* **11**, 748 (2015).
- [14] N. Xu, H. M. Weng, B. Q. Lv, C. E. Matt, J. Park, F. Bisti, V. N. Strocov, D. Gawryluk, E. Pomjakushina, K. Conder, N. C. Plumb, M. Radovic, G. Autès, O. V. Yazyev, Z. Fang, X. Dai, T. Qian, J. Mesot, H. Ding, and M. Shi, *Nat. Commun.* **7**, 11006 (2016).
- [15] A. A. Burkov, M. D. Hook, and L. Balents, *Phys. Rev. B* **84**, 235126 (2011).
- [16] G. Bian, T.-R. Chang, R. Sankar, S.-Y. Xu, H. Zheng, T. Neupert, C.-K. Chiu, S.-M. Huang, G. Chang, I. Belopolski, D. S. Sanchez, M. Neupane, N. Alidoust, C. Liu, B. Wang, C.-C. Lee, H.-T. Jeng, C. Zhang, Z. Yuan, S. Jia, A. Bansil, F. Chou, H. Lin, and M. Z. Hasan, *Nat. Commun.* **7**, 10556 (2016).
- [17] C. Fang, H. Weng, X. Dai, and Z. Fang, *Chin. Phys. B* **25**, 117106 (2016).
- [18] T. Liang, Q. Gibson, M. N. Ali, M. Liu, R. J. Cava, and N. P. Ong, *Nat. Mater.* **14**, 280 (2015).
- [19] J. Xiong, S. Kushwaha, J. Krizan, T. Liang, R. J. Cava, and N. P. Ong, *EPL Europhys. Lett.* **114**, 27002 (2016).
- [20] C. Shekhar, A. K. Nayak, Y. Sun, M. Schmidt, M. Nicklas, I. Leermakers, U. Zeitler, Y. Skourski, J. Wosnitza, Z. Liu, Y. Chen, W. Schnelle, H. Borrmann, Y. Grin, C. Felser, and B. Yan, *Nat. Phys.* **11**, 645 (2015).
- [21] N. J. Ghimire, Y. Luo, M. Neupane, D. J. Williams, E. D. Bauer, and F. Ronning, *J. Phys.: Condens. Matter* **27**, 152201 (2015).
- [22] Z. Wang, Y. Zheng, Z. Shen, Y. Lu, H. Fang, F. Sheng, Y. Zhou, X. Yang, Y. Li, C. Feng *et al.*, *Phys. Rev. B* **93**, 121112(R) (2016).

- [23] F. Arnold, C. Shekhar, S.-C. Wu, Y. Sun, R. D. dos Reis, N. Kumar, M. Naumann, M. O. Ajeesh, M. Schmidt, A. G. Grushin, J. H. Bardarson, M. Baenitz, D. Sokolov, H. Borrmann, M. Nicklas, C. Felser, E. Hassinger, and B. Yan, *Nat. Commun.* **7**, 11615 (2016).
- [24] X. Huang, L. Zhao, Y. Long, P. Wang, D. Chen, Z. Yang, H. Liang, M. Xue, H. Weng, Z. Fang, X. Dai, and G. Chen, *Phys. Rev. X* **5**, 031023 (2015).
- [25] Y. Zhao, H. Liu, C. Zhang, H. Wang, J. Wang, Z. Lin, Y. Xing, H. Lu, J. Liu, Y. Wang, S. M. Brombosz, Z. Xiao, S. Jia, X. C. Xie, and J. Wang, *Phys. Rev. X* **5**, 031037 (2015).
- [26] C.-L. Zhang, S.-Y. Xu, I. Belopolski, Z. Yuan, Z. Lin, B. Tong, G. Bian, N. Alidoust, C.-C. Lee, S.-M. Huang, T.-R. Chang, G. Chang, C.-H. Hsu, H.-T. Jeng, M. Neupane, D. S. Sanchez, H. Zheng, J. Wang, H. Lin, C. Zhang, H.-Z. Lu, S.-Q. Shen, T. Neupert, M. Z. Hasan, and S. Jia, *Nat. Commun.* **7**, 10735 (2016).
- [27] A. A. Zyuzin and A. A. Burkov, *Phys. Rev. B* **86**, 115133 (2012).
- [28] J. Park, G. Lee, F. Wolff-Fabris, Y. Y. Koh, M. J. Eom, Y. K. Kim, M. A. Farhan, Y. J. Jo, C. Kim, J. H. Shim *et al.*, *Phys. Rev. Lett.* **107**, 126402 (2011).
- [29] Y. Feng, Z. Wang, C. Chen, Y. Shi, Z. Xie, H. Yi, A. Liang, S. He, J. He, Y. Peng, X. Liu, Y. Liu, L. Zhao, G. Liu, X. Dong, J. Zhang, C. Chen, Z. Xu, X. Dai, Z. Fang, and X. J. Zhou, *Sci. Rep.* **4**, 5385 (2014).
- [30] K. Wang, D. Graf, L. Wang, H. Lei, S. W. Tozer, and C. Petrovic, *Phys. Rev. B* **85**, 041101(R) (2012).
- [31] G. Lee, M. A. Farhan, J. S. Kim, and J. H. Shim, *Phys. Rev. B* **87**, 245104 (2013).
- [32] J. B. He, Y. Fu, L. X. Zhao, H. Liang, D. Chen, Y. M. Leng, X. M. Wang, J. Li, S. Zhang, M. Q. Xue, C. H. Li, P. Zhang, Z. A. Ren, and G. F. Chen, *Phys. Rev. B* **95**, 045128 (2017).
- [33] J. Y. Liu, J. Hu, Q. Zhang, D. Graf, H. B. Cao, S. M. A. Radmanesh, D. J. Adams, Y. L. Zhu, G. F. Cheng, X. Liu, W. A. Phelan, J. Wei, M. Jaime, F. Balakirev, D. A. Tennant, J. F. DiTusa, I. Chiorescu, L. Spinu, and Z. Q. Mao, *Nat. Mater.* **16**, 905 (2017).
- [34] J. Liu, J. Hu, H. Cao, Y. Zhu, A. Chuang, D. Graf, D. J. Adams, S. M. A. Radmanesh, L. Spinu, I. Chiorescu, and Z. Mao, *Sci. Rep.* **6**, 30525 (2016).
- [35] Y.-Y. Wang, S. Xu, L.-L. Sun, and T.-L. Xia, *Phys. Rev. Mater.* **2**, 021201(R) (2018).
- [36] M. A. Farhan, G. Lee, and J. H. Shim, *J. Phys.: Condens. Matter* **26**, 042201 (2014).
- [37] C. Yi, S. Yang, M. Yang, L. Wang, Y. Matsushita, S. Miao, Y. Jiao, J. Cheng, Y. Li, K. Yamaura, Y. Shi, and J. Luo, *Phys. Rev. B* **96**, 205103 (2017).
- [38] S. Borisenko, D. Evtushinsky, Q. Gibson, A. Yaresko, K. Koepernik, T. Kim, M. Ali, J. van den Brink, M. Hoesch, A. Fedorov, E. Haubold, Y. Kushnirenko, I. Soldatov, R. Schäfer, and R. J. Cava, *Nat. Commun.* **10**, 3424 (2019).
- [39] Q. Xu, Z. Song, S. Nie, H. Weng, Z. Fang, and X. Dai, *Phys. Rev. B* **92**, 205310 (2015).
- [40] L. M. Schoop, M. N. Ali, C. Straßler, A. Topp, A. Varykhalov, D. Marchenko, V. Duppel, S. S. Parkin, B. V. Lotsch, and C. R. Ast, *Nat. Commun.* **7**, 11696 (2016).
- [41] N. Kumar, K. Manna, Y. Qi, S.-C. Wu, L. Wang, B. Yan, C. Felser, and C. Shekhar, *Phys. Rev. B* **95**, 121109(R) (2017).
- [42] J. Hu, Z. Tang, J. Liu, X. Liu, Y. Zhu, D. Graf, K. Myhro, S. Tran, C. N. Lau, J. Wei, and Z. Mao, *Phys. Rev. Lett.* **117**, 016602 (2016).
- [43] J. Hu, Y. L. Zhu, D. Graf, Z. J. Tang, J. Y. Liu, and Z. Q. Mao, *Phys. Rev. B* **95**, 205134 (2017).
- [44] L. M. Schoop, A. Topp, J. Lippmann, F. Orlandi, L. Muehler, M. G. Vergniory, Y. Sun, A. W. Rost, V. Duppel, M. Krivenkov, S. Sheoran, P. Manuel, A. Varykhalov, B. Yan, R. K. Kremer, C. R. Ast, and B. V. Lotsch, *Sci. Adv.* **4**, eaar2317 (2018).
- [45] R. Singha, A. Pariari, B. Satpati, and P. Mandal, *Phys. Rev. B* **96**, 245138 (2017).
- [46] R. Lou, J.-Z. Ma, Q.-N. Xu, B.-B. Fu, L.-Y. Kong, Y.-G. Shi, P. Richard, H.-M. Weng, Z. Fang, S.-S. Sun, Q. Wang, H.-C. Lei, T. Qian, H. Ding, and S.-C. Wang, *Phys. Rev. B* **93**, 241104(R) (2016).
- [47] M. M. Hosen, G. Dhakal, K. Dimitri, P. Maldonado, A. Aperis, F. Kabir, C. Sims, P. Riseborough, P. M. Oppeneer, D. Kaczorowski, T. Durakiewicz, and M. Neupane, *Sci. Rep.* **8**, 13283 (2018).
- [48] J. Hu, Y. Zhu, X. Gui, D. Graf, Z. Tang, W. Xie, and Z. Mao, *Phys. Rev. B* **97**, 155101 (2018).
- [49] M. Neupane, I. Belopolski, M. M. Hosen, D. S. Sanchez, R. Sankar, M. Szlowska, S.-Y. Xu, K. Dimitri, N. Dhakal, P. Maldonado, P. M. Oppeneer, D. Kaczorowski, F. Chou, M. Z. Hasan, and T. Durakiewicz, *Phys. Rev. B* **93**, 201104(R) (2016).
- [50] M. N. Ali, L. M. Schoop, C. Garg, J. M. Lippmann, E. Lara, B. Lotsch, and S. S. Parkin, *Sci. Adv.* **2**, e1601742 (2016).
- [51] R. Singha, A. K. Pariari, B. Satpati, and P. Mandal, *Proc. Natl. Acad. Sci.* **114**, 2468 (2017).
- [52] B.-B. Fu, C.-J. Yi, T.-T. Zhang, M. Caputo, J.-Z. Ma, X. Gao, B. Q. Lv, L.-Y. Kong, Y.-B. Huang, P. Richard, M. Shi, V. N. Strocov, C. Fang, H.-M. Weng, Y.-G. Shi, T. Qian, and H. Ding, *Sci. Adv.* **5**, eaau6459 (2019).
- [53] H. Pan, B. Tong, J. Yu, J. Wang, D. Fu, S. Zhang, B. Wu, X. Wan, C. Zhang, X. Wang, and F. Song, *Sci. Rep.* **8**, 9340 (2018).
- [54] J. Y. Liu, J. Yu, J. L. Ning, H. M. Yi, L. Miao, L. J. Min, Y. F. Zhao, W. Ning, K. A. Lopez, Y. L. Zhu, T. Pillsbury, Y. B. Zhang, Y. Wang, J. Hu, H. B. Cao, F. Balakirev, F. Weickert, M. Jaime, Y. Lai, K. Yang, J. W. Sun, N. Alem, V. Gopalan, C. Z. Chang, N. Samarth, C. X. Liu, R. D. McDonald, and Z. Q. Mao, *arXiv:1907.06318*.
- [55] H. Masuda, H. Sakai, M. Tokunaga, Y. Yamasaki, A. Miyake, J. Shiozaki, S. Nakamura, S. Awaji, A. Tsukazaki, H. Nakao, Y. Murakami, T. Arima, Y. Tokura, and S. Ishiwata, *Sci. Adv.* **2**, e1501117 (2016).
- [56] Y. Zhu, T. Zhang, J. Hu, J. Kidd, D. Graf, X. Gui, W. Xie, M. Zhu, X. Ke, H. Cao, Z. Fang, H. Weng, and Z. Mao, *Phys. Rev. B* **98**, 035117 (2018).
- [57] Y. U. E. Cheng-Yang, *Chin. J. Inorg. Chem.* **11**, 025 (2011).
- [58] I. M. Lifshitz and A. M. Kosevich, *Sov Phys JETP* **2**, 636 (1956).
- [59] D. Shoenberg, *Magnetic Oscillations in Metals* (Cambridge University Press, Cambridge, 2009).
- [60] J. Hu, S.-Y. Xu, N. Ni, and Z. Mao, *Annu. Rev. Mater. Res.* **49**, 207 (2019).
- [61] M. V. Kartsovnik, *Chem. Rev.* **104**, 5737 (2004).